Measurement 202 (2022) 111852

Contents lists available at ScienceDirect

Measurement

journal homepage: www.elsevier.com/locate/measurement

Internal imaging of concrete fracture based on elastic waves and ultrasound computed tomography

Monika Zielińska [a], Magdalena Rucka [b,*]

[a] Department of Technical Fundamentals of Architectural Design, Faculty of Architecture, Gdańsk University of Technology, Narutowicza 11/12, 80-233 Gdańsk, Poland
[b] Department of Mechanics of Materials and Structures, Faculty of Civil and Environmental Engineering, Gdańsk University of Technology, Narutowicza 11/12, 80-233 Gdańsk, Poland

ARTICLE INFO

Keywords:
Fracture monitoring
Non-destructive testing
Damage imaging
Ultrasound tomography
X-ray micro-computed tomography

ABSTRACT

The condition assessment of concrete structures belongs to the greatest challenges of non-destructive testing. Monitoring the fracture process of concrete and detecting cracks at the earliest possible stage is a vital aspect to ensure the safety of civil engineering objects. The use of ultrasound tomography enables imaging the internal structure of a tested element. This study aims at the visualization of fracture damage in concrete cubes. The tests are performed on samples made of plain concrete and concrete with fibres. The main contribution of this work is the study of the application of ultrasound transmission tomography to imaging cracks in concrete prisms before and after mechanical degradation in a wedge splitting test. A novel method of determination of the time-of-flight of a wave propagating from a transmitter to a receiver is introduced. The effectiveness of the imaging of fracture damage obtained using ultrasound tomography is proved by X-ray micro-computed tomography.

1. Introduction

Concrete, as a brittle material with high compressive and low tensile strength, is very prone to cracking. The fracture process is complex and begins with microcracks which then gradually merge into macroscopic cracks and may further lead to the complete failure of a concrete structure. Therefore, it is so important to detect cracks at the earliest possible stage to prevent a possible construction disaster. Experimental research has shown that the development of cracks in concrete under load depends mainly on the internal structure of the element, i.e. the volume of mortar and aggregate, porosity, size, shape and roughness of the aggregate. Consequently, it is very difficult to predict the exact course of the cracks. This is the reason why the characterization and evaluation of the fracture process are so important and various non-destructive testing (NDT) techniques are engaged for this challenging task.

Nowadays, the imaging of the internal structure of engineering objects focused on the evaluation of the fracture process has become a great challenge for modern damage detection and structural health monitoring systems. Undoubtedly, one of the most efficient methods for exact internal imaging is using X-ray micro-computed tomography (micro-CT). Micro-CT enables obtaining high-resolution images that provide a realistic microstructure of a wide range of materials. Many successful applications of characterization of concrete fracture have been made using micro-CT, including examples of mechanical degradation such as bending [1], compression [2,3], splitting [4,5] as well as corrosion-induced cracks [6]. Micro-CT has been also used to test fibre-reinforced concrete to determine the distribution, amount, shape or type of fibres [7–11]. Results of micro-CT imaging have been widely used to generate concrete mesoscale models including cement matrix, aggregates, macro-pores and interfacial transitional zones between the aggregate and cement matrix. Various finite element and discrete element models [12–16] have been used for numerical modelling of damage in concrete to study behaviour at different stages of fracture. Most often research using micro-CT relies on scanning samples before and after mechanical degradation (e.g. [9]). However, the newest investigations are devoted to continuous micro-CT scanning of concrete samples under progressive compressive or bending loading, e.g. [14,17,18]. It should be noted that despite the high efficiency, the method of computed microtomography also has some drawbacks. The main disadvantage is the limitation of the use of the method on real objects, due to the need to conduct the test in a special measuring apparatus.

The limitations of early detection of cracks on a real object are

* Corresponding author.
E-mail addresses: magdalena.rucka@pg.edu.pl, monika.zielinska@pg.edu.pl (M. Rucka).

https://doi.org/10.1016/j.measurement.2022.111852
Received 30 June 2022; Received in revised form 10 August 2022; Accepted 26 August 2022
Available online 6 September 2022

overcome by methods based on elastic waves. One of such method is ultrasound tomography based on information collected from waves propagating through the tested element. Data collection devices are compact and can be successfully used in situ. In concrete elements, tomography is used to locate the reinforcement [19,20], inclusions of foreign materials [19,21,22] or to detect debonding of the reinforcement [23]. Ultrasound tomography also allows for the detection and imaging of cracks in concrete or reinforced concrete elements [24,25]. Research related to the detection of cracks has been carried out by Chai et. al [26]. They developed an algorithm to facilitate simultaneous tracking and distribution of the amplitude factor in a 3D model. They used the obtained results for the tomographic reconstruction of elements with damages imitating fracture. Niu et al. [27] conducted an integrated study for concrete structures using Bayesian theory and ultrasound tomography. In one of the tested samples, they imitated the defect in the form of cracks. However, works for studying a fracture process using ultrasound computed tomography are still rare. Haach and Juliani [28] examined concrete prisms before and after damage, showing a decrease in the velocity of wave propagation in the elements after destruction. Perkowski and Tatara [29] considered imaging brittle damage in concrete beams subjected to three-point bending. They determined the real paths of ultrasonic waves using the graph theory and Dijkstra's algorithm. Basu et al. [30] used ultrasound tomography to initially identify damaged critical areas in a reinforced concrete element. The tests were carried out on a laboratory model of the girder with different load levels, indicating the development of damage in some areas.

The paper deals with the visualisation of fracture damage in quasi-brittle materials on the example of concrete elements. The main contribution of this work is the study of the application of ultrasound transmission tomography to imaging cracks in concrete prisms before and after mechanical degradation. The results are presented for cubes made of plain concrete and concrete with steel and polymer fibres. To analyse the fracture phenomenon in a wedge splitting test, wave propagation velocity measurements were made. A novel starting point search method for the determination of the time-of-flight of an ultrasonic wave propagating from a transmitter to a receiver was proposed. Based on it, the distribution of the velocity of the elastic wave propagation within the tested element was determined and then precise tomographic maps were performed. The effectiveness of the imaging of fracture damage using ultrasound tomography was proved by images from X-ray micro-CT. The results obtained in this paper may be treated as an initial step toward in situ condition monitoring of concrete elements and imaging their internal structure.

2. Experimental investigations

2.1. Mixtures and specimens

The concrete mixture was composed of cement type CEM I 42.5R (380 kg/m^3), aggregate 0/2 mm (648 kg/m^3), aggregate 2/8 mm (426 kg/m^3), aggregate 8/16 mm (754 kg/m^3), water (165 kg/m^3), and super-plasticizer (0.8% of cement content). Three different mixtures were prepared. The first (mixture #1) was plane concrete. The two other mixtures (#2 and #3) were prepared based on mixture #1, adding to it two different types of fibres at the rate of 0.6% by the total volume of concrete. Mixture #2 contained 5.46 kg/m^3 polymer fibres with a length of 24 mm and a diameter of 0.45 mm, while mixture #3 contained 47.1 kg/m^3 steel fibres with a length of 25 mm and a diameter of 0.5 mm. Three 10 × 10 × 50 cm^3 concrete prisms were made of each mixture. Then, cubic specimens 7 × 7 × 7 cm^3 were cut from the prisms. In each of the cubes, a rectangular notch with a width of 4 mm and a depth of 15 mm was cut. These three specimens (cube #1 – made of plain concrete, cube #2 – made of concrete with polymer fibres, cube #3 – made of concrete with steel fibres) were investigated in the further part of the study (Fig. 1).

2.2. Experimental setup and procedure

The fracture process of the concrete cubes was investigated in the wedge splitting test (WST). The experimental setup and sample under testing are shown in Fig. 2a. During fracture, the cubes were supported on the linear support on the bottom and the steel wedge was inserted in the notch. The splitting test was carried out using a universal testing machine (UTM) Zwick/Roell Z10, with a constant displacement rate of 0.1 mm/min, until 2 mm displacement of the cross-head, which was achieved after 1200 s.

The time-force curves of the quasi-static splitting test are illustrated in Fig. 3. The peak values of the load were: 6.39 kN (cube #1), 5.7 kN (cube #2) and 8.02 kN (cube #3). The samples revealed different behaviour depending on the type of concrete mixture. For the cube made of plain concrete (cube #1), a sudden, quasi-brittle cracking occurred. The force corresponding to the 2 mm wedge displacement was 1.95% P_{max}. An increment in ductility is visible in cubes with fibres compared with a specimen made of plain concrete. Adding polymer fibres resulted in the post-cracking behaviour not so sudden as in the case of plain concrete. For cube #2, the force corresponding to the 2 mm wedge displacement was 10.14% P_{max}. A sample with steel fibres (cube #3) revealed a gradual decrease in force, amounting to 36.88% P_{max} for a 2 mm wedge displacement.

Before and after fracture in the splitting test, the elastic waves were excited and recorded using the multilayer piezoelectric transducers NAC2024, manufactured by Noliac. The excitation was a one-cycle sine wave with a frequency of 100 kHz, modulated by the Hann window. The AFG3022C arbitrary waveform generator and the AB A400DI high voltage amplifier were used to generate the excitation. Wave propagation signals were registered using the PicoScope 4824 digital oscilloscope.

In the survey, twenty-four transducers were attached to the specimen surface, in the middle of the sample height (i.e. at a height of 35 mm), as shown in Fig. 2b. Twelve transmitters (T_1–T_{12}) were placed on two adjacent walls (i.e. six transmitters on each wall). The first transmitter was attached at a distance of 5 mm from the edge of the sample, and the

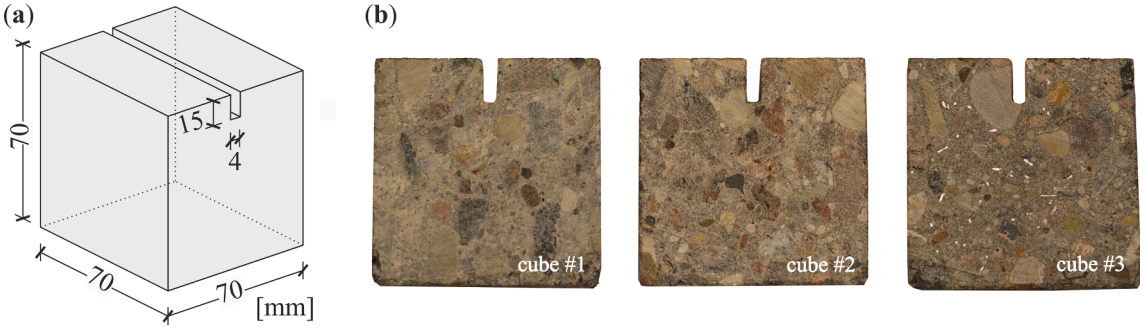

Fig. 1. The geometry of the concrete specimen (a) and front view of cubes #1, #2 and #3 (b).

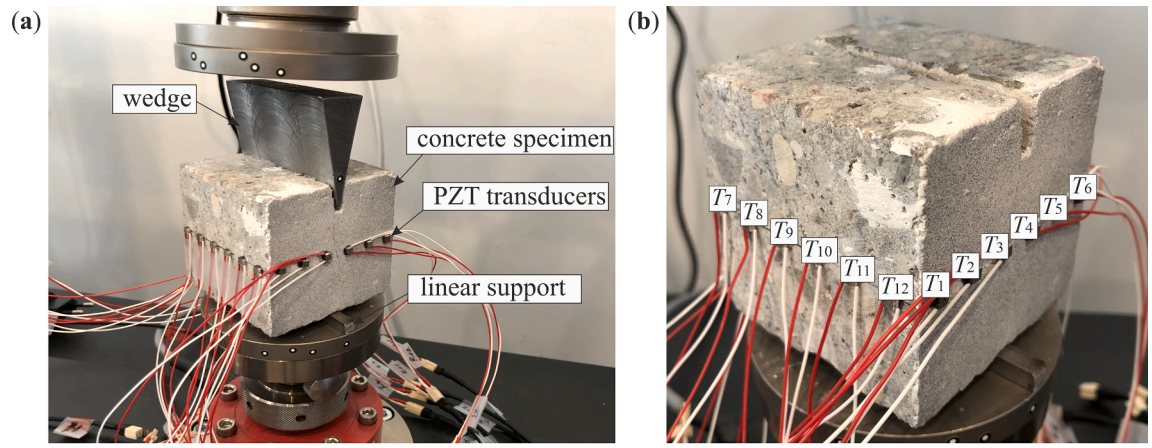

Fig. 2. Experimental setup: specimen under splitting test (a); location of piezoelectric transducers (b).

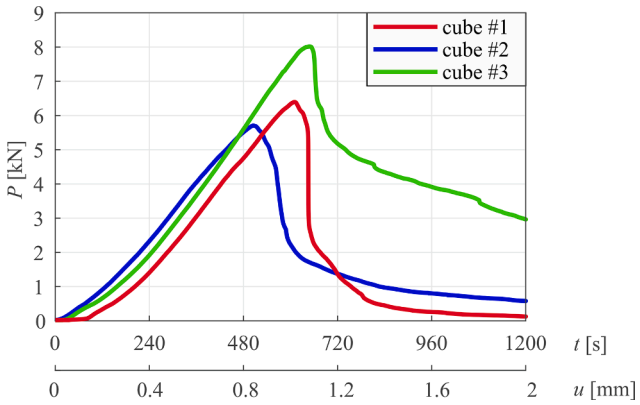

Fig. 3. Load curves for cubes #1 – #3 with marked stages B and C of measurements.

others at a distance of 12 mm. Twelve receivers (R_1–R_{12}) were arranged on two opposite walls in the same way. During a single measurement, one of the transmitters excited a wave, while six receivers localized on the opposite side registered time histories. A typical set of signals is given in Fig. 4 (the excitation signal given by transmitter T_1 and the exemplary signals recorded by receivers R_1–R_6 located on the opposite wall). The measurements were repeated twelve times (using subsequent transmitters), so a total of 72 signals were collected along the paths shown in Fig. 5 for further imaging using ultrasonic tomography.

The ultrasonic measurements were repeated four times for each specimen. The first ultrasonic survey was carried out for the unloaded, undamaged cube (stage A). The second ultrasonic survey (stage B) was made for a cube under preload with a value of 20 N. Then the survey was repeated after splitting when the testing machine achieved a displacement of 2 mm (stage C). The last survey (stage D) was performed after unloading the sample. All wave propagation signals used in this paper are available in [31].

3. Ultrasonic transmission tomography

3.1. Procedure for automated time-of-flight determination

The crucial element required for ultrasonic tomography imaging is the determination of the time-of-flight (TOF) along individual paths. The time-of-flight is measured as the distance between two points of a waveform, defining the starting point of the input and output signals, respectively. Identification of the starting point of the signal can be often troublesome due to insufficient signal quality, ambiguity or noise. This point can be determined automatically or manually by indicating it in each signal separately. In the case of ultrasound travel-time tomography, the amount of collected data is very large, and the manual search for the starting point in each signal can become very long and ambiguous. Manual search for a starting point is subjective which was proved by Cescatti et al. [32] by comparing the position of the starting points determined by seven independent expert operators. Since the determination of the time-of-flight directly affects the ultrasound tomography maps, this subjective factor should be eliminated. For this reason, automated methods of measurement data processing are preferred, which allow for the quick collection of the TOFs. The basic automated approach for determining TOFs is the use of threshold methods. They consist in identifying the place in the signal where a certain threshold is exceeded. However, these methods are susceptible to noise and signal interference. In 1981 Beck [33] proposed the determination of TOF by the signal correlation method. This technique measures the similarity of two signals and the result is the time shift which gives the greatest similarity of both signals. Then, improved correlation methods such as phase-correlation or cross-correlation were proposed [34]. Unfortunately, the correlation method can give inconclusive results due to noise, mode conversion or spreading. An automated technique for the determination of the TOF was proposed by Cescatti et al. [32]. The developed algorithm uses a geometrical method to detect the starting point of the input signal and an adaptive threshold method for the identification of the starting point of the output signal. Rodríguez-Mariscal et al. [35] introduced a new automated procedure for the TOF identification based on a set of criteria including noise analysis, signal shapes and statistical variables. Fang et al. [36] introduced a technique for the time-of-flight determination using the multiple-zero-crossing technique.

This paper proposes an original method of determining the TOF, called the starting point search (SPS). The method was developed based on the analysis of the wave signal and the problems that may arise in finding the starting point. The scheme of the method is shown in Fig. 6. Observation of the initial, undisturbed part of the signal allows the identification of noise. This is necessary to specify the input parameter D_{dev} which value must be greater than the noise level. The identification of the starting point in the proposed approach begins with the determination of the signal envelope. The first point with a value of amplitude greater than the specified D_{dev} (point R_1) is plotted on the graph. This is the first point determining the position of the line r. The second point that defines the course of this line is point R_2. This is the point of change of monotonicity of the envelope function, located to the left of point R_1. The place of intersection of line r with the x-axis determines the location of point T_1. The next step is to find the first upper (x_u, y_u) and bottom peaks (x_b, y_b), with a value on the x-axis greater than T_1. Due to the

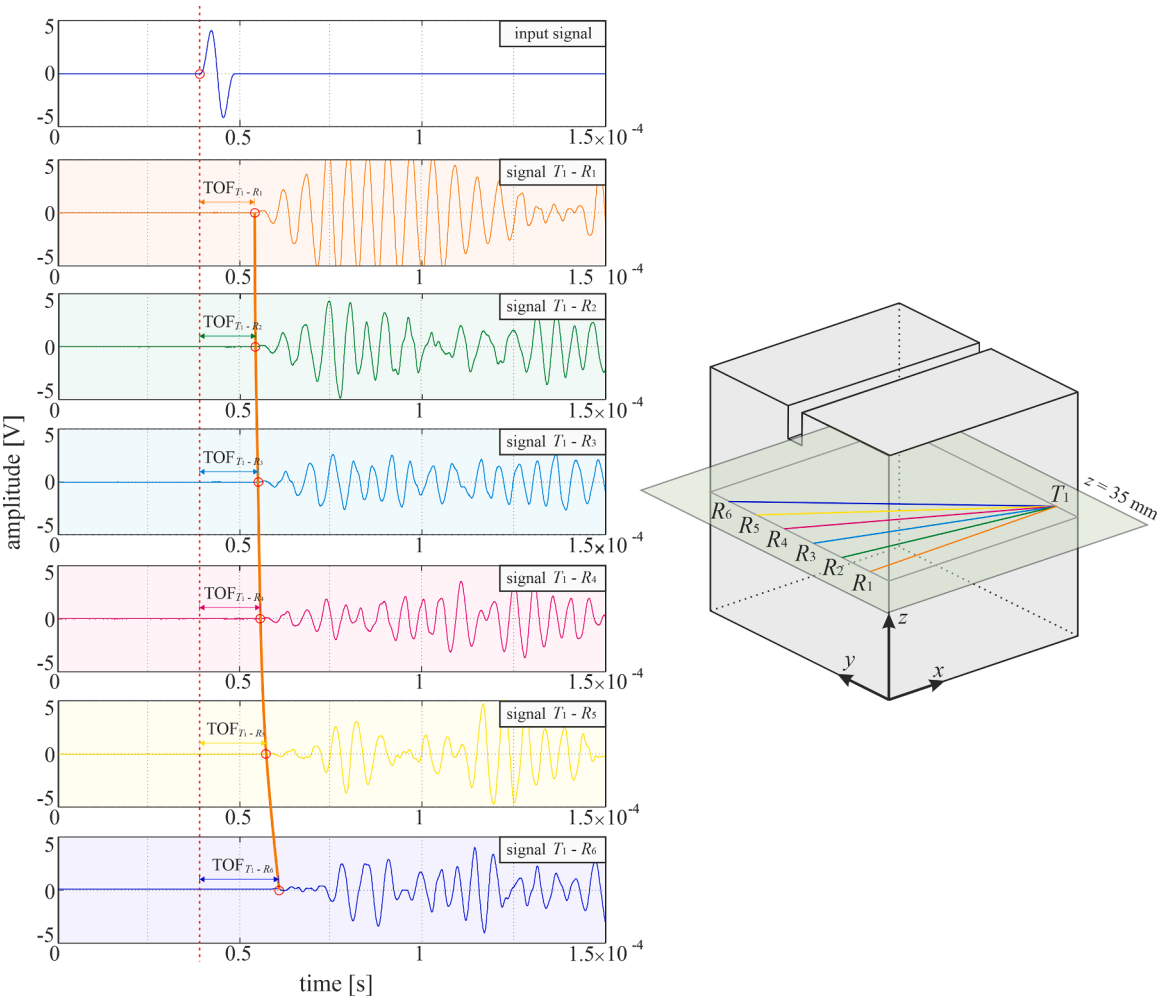

Fig. 4. Typical ultrasonic wave signals propagating between transmitter (T_1) and receivers (R_1–R_6).

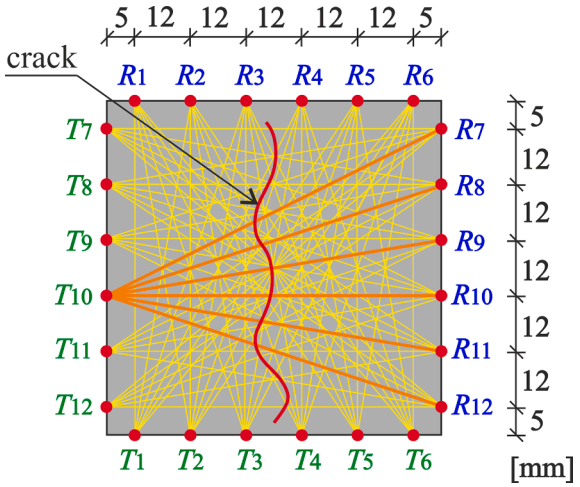

Fig. 5. Cross-section of a concrete cube with the configuration of transducers and measurement paths.

possibility of changing the phase of the signal, the peaks are labelled as P_1 (first peak) and P_2 (second peak), respectively. In order to avoid the error, the algorithm checks if there is no peak in front of the determined peak P_1, the value of which was incorrectly read as noise. These extra points are searched at the distance d, measured to the left of the first peak P_1 ($x_{u/b}$):

$$d = x_{u/b} - 2(|x_u - x_b|) \quad (1)$$

Then, from the determined point P_1, moving point by point along the abscissa axis, the first point whose amplitude is lower than the noise average is searched for. This point is referred to as the N signal starting point. Average noise is calculated for a signal propagating in time $< 0, T_1 >$.

The correctness of the proposed SPS method was checked by comparing the results with the method based on determining the Akaike Information Criterion (AIC). For the time series $\times$ of length S, the value of the AIC function is calculated from the formula [37]:

$$\mathrm{AIC}(k) = k\log(var(x[1,k])) + (S-k-1)\log(var(x[k+1,S])) \quad (2)$$

where k is the range over the entire time period, S is the number of data samples in the received signal, $x[1, k]$ and $x[k + 1, S]$ are signal segments before and after the k-th point. The terms $var(x[1, k])$ and $var(x[k + 1,S])$ represent the variances of two signal segments. The AIC method works properly if the ratio of signal amplitude to noise is large enough and signal excitation is visible.

An example of estimating the starting point position using the AIC function is shown in Fig. 7. The AIC value was initially calculated from the entire signal (AIS 1st). In order to obtain a reliable estimation result, a limited time window should be defined. In the study, the time window was 20 μs long, assuming 10 μs on each side of the minimum point of the AIS 1st function. Then AIC calculations were repeated for the adaptive window (AIC 2nd). The close-up in Fig. 7 compares the position of the starting points of the signal determined by the SPS, AIC 1st and AIC 2nd

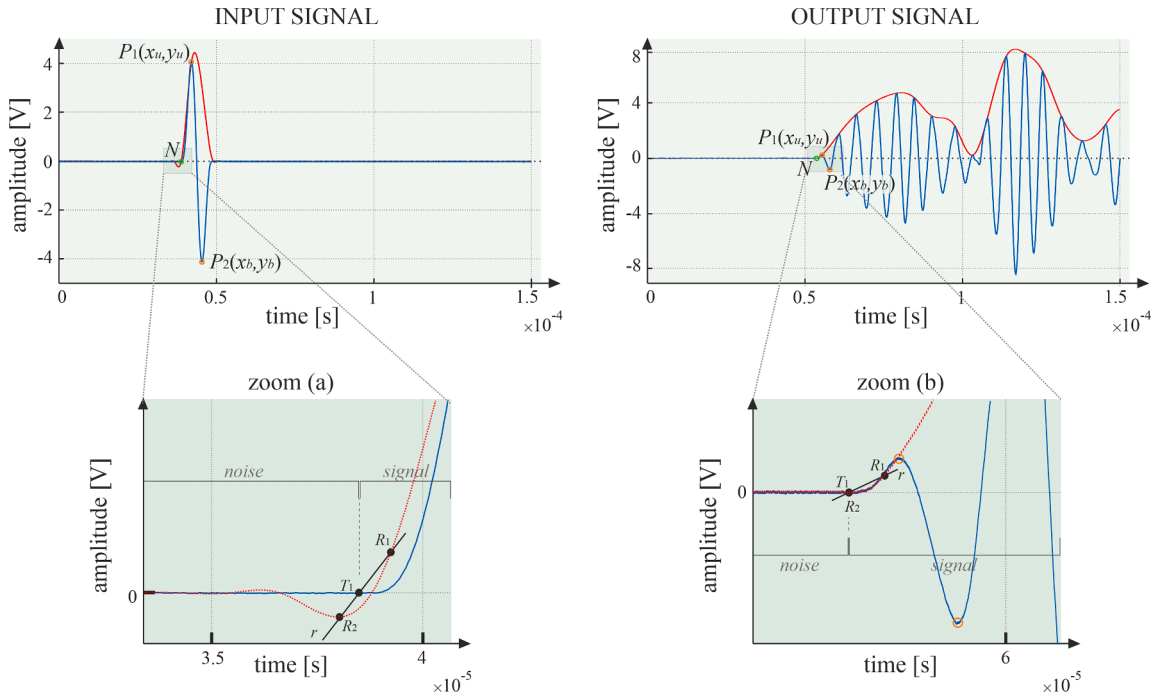

Fig. 6. Scheme of finding the starting point of a signal using the SPS method.

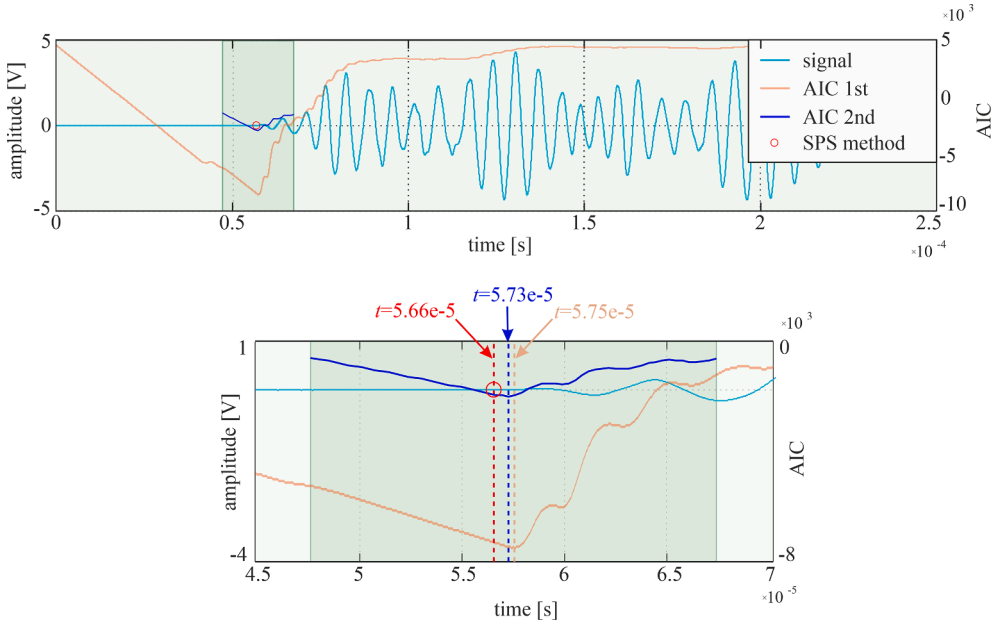

Fig. 7. Comparison of determining the position of the starting point of the function by the SPS, AIC 1st and AIC 2nd methods.

methods. The results are not identical. It can be observed that the AIC method indicates several local minima depending on the selected time window. This may result in an incorrect estimation of the starting point of the signal. It should be also noted that the proposed SPS method is independent of the selected time window.

The results obtained by SPS, AIC 1st and AIC 2nd methods are summarized in the bar graph (Fig. 8). The signals collected from three undamaged samples (stage A) made of plain concrete (cube #1), concrete with polymer fibres (cube #2) and concrete with steel fibres (cube #3) were analyzed. Each of the graphs compares the position of the starting points of the waves propagating from the transmitters T_1-T_{12} to the receivers R_1-R_{12}. The average difference between the results obtained by the SPS method and the AIC 1st and AIC 2nd methods was measured. These differences for cube #1 were 1.37% and 1.39%, for cube #2 – 1.85% and 1.44% and for cube #3 – 2.00% and 1.95%, respectively. These differences can be considered as minor, and the SPS method of identifying the position of the starting point of the signal as correct.

3.2. *Algorithm of ultrasound tomography*

Transmission ultrasound tomography is based on information obtained from waveforms propagating in an examined medium. The ultrasonic wave induced by a transmitter passes through a tested element

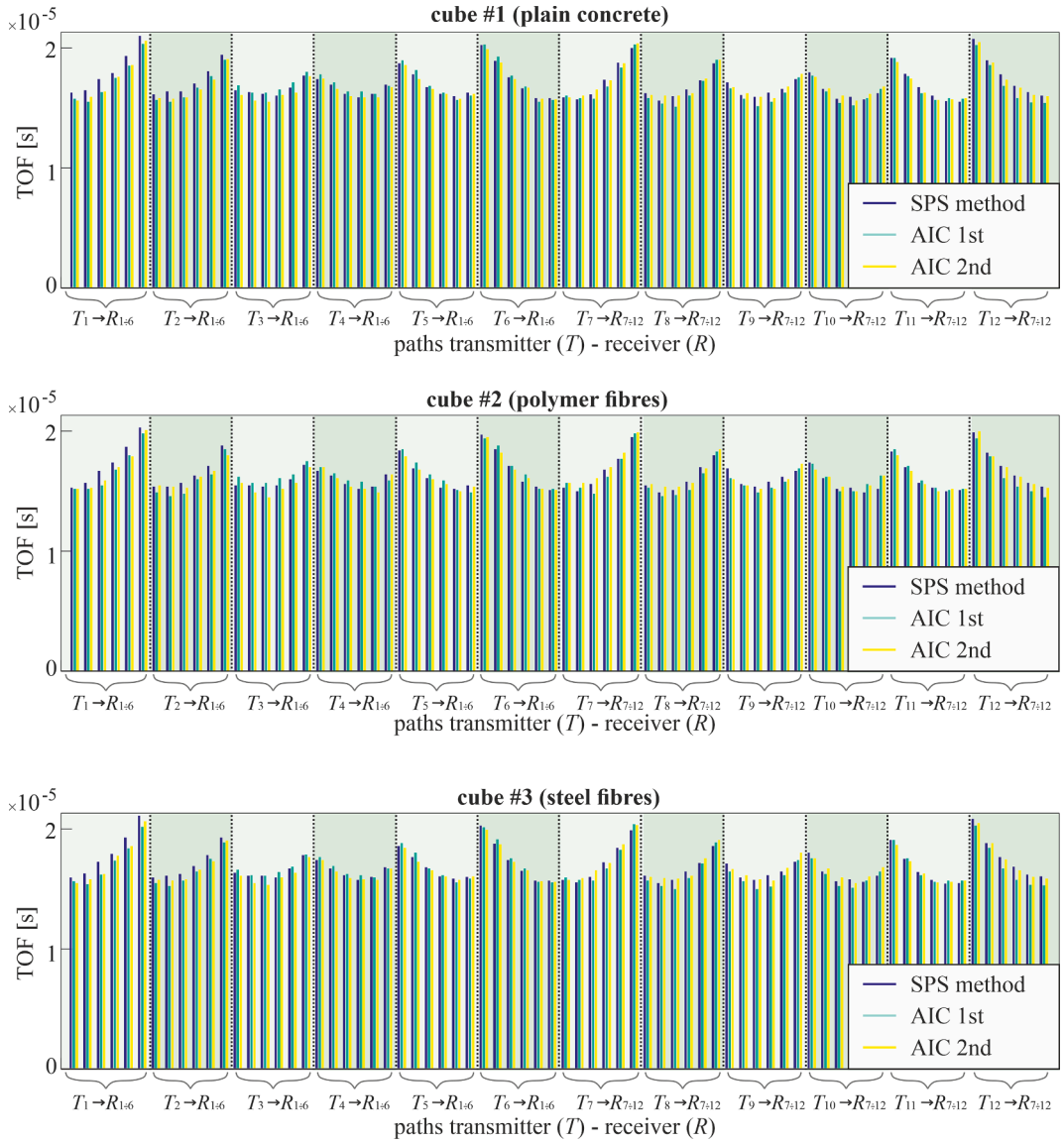

Fig. 8. TOF comparison for signals propagating from transmitters (T_1-T_{12}) to receivers (R_1-R_{12}) determined by SPS, AIC 1st and AIC 2nd methods.

and reaches the receivers, resulting in the collection of a set of signals. A typical set of signals registered in this study is shown in Fig. 4. The measurement is then repeated sequentially for each transmitter. A sufficiently large amount of collected measurement data enables the reconstruction of the internal structure of the element. A typical feature used in reconstruction is the time-of-flight of the ultrasonic wave from the transmitter to the receiver, which is delayed or accelerated by caverns, voids, discontinuities or other inclusions in the wave path.

To recreate the internal structure of an object, the examined plane is divided into a grid of n discrete elements (pixels), which is then analysed. Following the basic tomography approach, it is assumed that paths of known length traced between transmitters and receivers are straight lines. Since the path of each signal passes through a different set of discrete elements, the total propagation time T of any i-th path is the sum of the travel times through each of j-th element. On the basis of wave propagation velocity (V_j) or its inverse, defined as slowness (S_j) and the transition way of the i-ray through the j-element (L_{ij}), the time of the wave passing through this element can be calculated:

$$T_i = \sum_{j=1}^{n} \frac{L_{ij}}{V_j} = \sum_{j=1}^{n} L_{ij} S_j, \; i = 1, 2, 3, \ldots, m, \; j = 1, 2, 3, \ldots, n \tag{3}$$

where i is the number of rays that ranges from 1 to m, j is the number of discrete elements that ranges from 1 to n.

The above set of equations is usually overdetermined in computed tomography problems. It can be efficiently solved using techniques such as ART – Algebraic Reconstruction Technique [38], MART – Multiplicative Algebraic Reconstruction Technique [39], SIRT – Simultaneous Iterative Reconstructive Technique [40] or OLS – Ordinary Least Squares [28]. In this study, the ART method was used, which is an iterative method of searching for a solution. In the first step of the iterative process, each discrete element is assigned a value, usually the average velocity value of the collected signals. Then, the iteration process is started, according to the equation [40]:

$$S_j^{(k)} = S_j^{(k-1)} + \frac{L_{ij} \Delta T_i}{\sum_{j=1}^{n} L_{ij}^2} \tag{4}$$

where ΔT_i is the difference between the time of the original projection and the rebuilding time. The system of equations is iteratively solved until the reconstructed travel time reaches the measured travel time, with an established error.

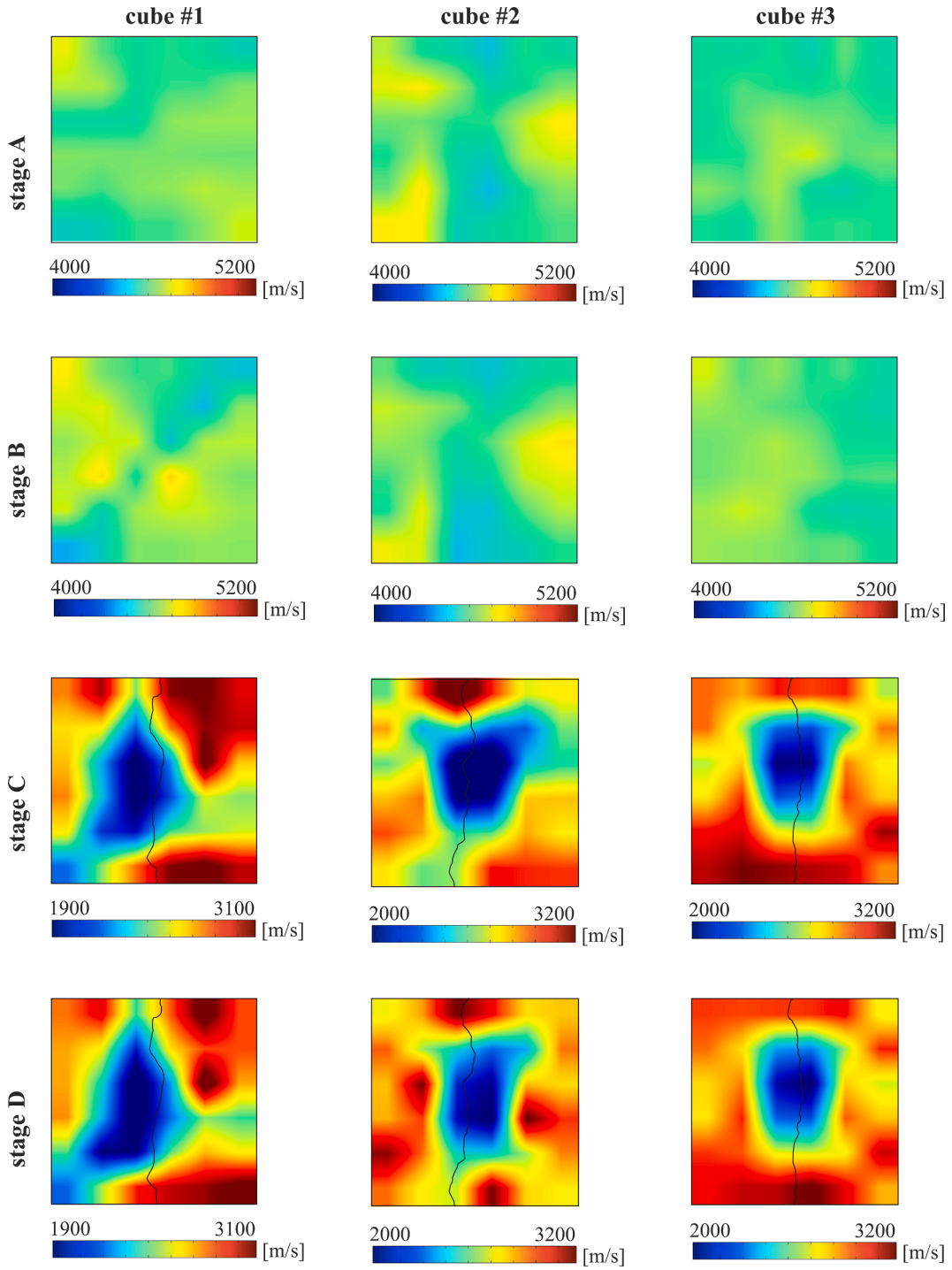

Fig. 9. Tomographic velocity images of three tested cubes (#1 – plain concrete, #2 – concrete with polymer fibre, #3 – concrete with steel fibres) at four stages (A – before loading, B – with 20 N preload, C – damaged, at the end of the splitting process, loaded, D – after unloading).

4. Results of ultrasound tomography

The ultrasonic tomography images are shown in Fig. 9. The reconstructed velocity maps were obtained using TOFs calculated based on the SPS method. The results are summarized for three samples made of plain concrete (cube #1), concrete with polymer fibres (cube #2) and concrete with steel fibres (cube #3). The maps were prepared for four stages: for the unloaded cube (stage A), for a cube under preload with a value of 20 N (stage B), after splitting when the testing machine achieved a displacement of 2 mm (stage C) and after unloading the sample (stage D). Each of them is presented in Fig. 9 in the same range of the scale so that they can be objectively compared. The maps for the unloaded cubes (stage A) and the cubes under preload with a value of 20 N (stage B) are very similar. It can be concluded that the application of such a small force did not change the speed of wave propagation in the concrete. There were also no clear differences observed in the tomographic images between the plain concrete and concrete with fibres. At the same time, significant differences can be noticed for the element before (stages A and B) and after destruction (C and D). For stages C and D, the fracture is visualized as a place with a reduced wave propagation

velocity. The damage course is similar for each concrete cube due to the failure characteristics. The maps obtained for individual samples after splitting, when the testing machine achieved a displacement of 2 mm (stage C) and after unloading the sample (stage D) are similar, however, one can observe that the areas with reduced velocity in stage D are smaller than in stage C as a result of crack closure after unloading of samples.

The ultrasound tomography maps were verified by comparing them with the results obtained from X-ray micro-computed tomography. Due to the use of micro-CT scanning, it was possible to see the inside of the tested specimens. The scans were carried out for specimens #1 to #3 before (stage A) and after (stage D) splitting tests with the SkyScan 1173 micro-CT scanner. After reconstruction, it was possible to obtain images of sections in the middle of the sample height, as in the ultrasonic test. X-ray tomography allowed for accurate visualization of the internal meso-/microstructure of concrete cubes, as shown in Fig. 10. The scans show the shape, size and distribution of aggregate and empty air spaces. In the case of the sample with steel fibres (cube #3), their arrangement can be observed. The exact course of the crack due to splitting is clearly visible in images made for stage D. The crack from micro-CT was then accurately marked on ultrasound tomography images. Comparing the results of the two methods of imaging the inside of the sample, one can notice that ultrasound tomography maps (Fig. 9) are not such precise as images from micro-CT (Fig. 10). It should be noted, however, that in the ultrasound tomographic velocity images, the areas with reduced wave propagation velocities coincide with the real course of the cracks, which proves the applicability of the ultrasound tomographic technique in detecting and imaging fracture damage. In addition, the superiority of the ultrasound tomography technique in the practical issues of civil engineering is related to the possibility of its application in situ and thus overcoming the significant limitation of microtomography resulting from the use of a scanning device in laboratory conditions.

The quantitative analysis of the average apparent velocities of ultrasonic waves propagating from transmitters T_1-T_{12} to six receivers located on the opposite wall is given in Table 1. The results are presented for each tested concrete sample at different stages (A to D). It can be noted that the velocities in cubes before failure (stages A and B) were of a similar range, regardless of the location of the transmitter, while after the splitting failure (stages C and D), there were significant differences in the velocities collected for the transmitters arranged in a plane perpendicular (transmitters T_1-T_6) and parallel (T_7-T_{12}) to the main plane of destruction. Wave rays propagating from transmitters located on the horizontal plane did not always pass through the destruction, so the average velocity was higher. Waves coming from transmitters located on a vertical wall always crossed the crack, which significantly reduced the average velocity of the wave.

Table 1 is summarized by listing the minimum, maximum and average velocity for each stage. The propagation velocity of an elastic wave for unloaded samples (stage A) and samples under preload with a value of 20 N (stage B) was almost the same. After the fracture, at stages C and D velocities were similar, however, a slight but noticeable increase in velocity can be observed in stage D compared to stage C, due to sample unloading and crack closure. The average velocity of waves propagated in the sample made of plain concrete was 4631.4 m/s and 4634.3 m/s for stages A and B, respectively. This value decreased significantly after cracking and amounted to 3051.4 m/s and 3092.6 m/s for stages C and D, respectively. Similar behaviour was observed for cubes with polymer fibres where the average velocity of 4609.3 m/s (stage A) and 4586.8 m/s (stage B) decreased to the values of 2937.2 m/s (stage C) and 2957.9 m/s (stage D). For an element with steel fibres, the average initial velocity was 4643.4 m/s and 4633.1 m/s (stages A and B) and it decreased after failure to 3035.5 m/s and 3192.2 m/s (stages C and D).

The analysis of the average velocity of propagating waves in cubes made of different mixtures brought the information that the highest velocity was in concrete with steel fibres and the lowest in concrete with polymer fibres. Noteworthy is the difference Δv between the value of the maximum and minimum velocity for the unloaded element (stage A). The difference was the smallest for the element made of plain concrete and amounted to 135.8 m/s. For the element with polymer fibres, the difference increased to 187.9 m/s, and for an element with steel fibres, the value was 289.0 m/s. This proves the strong influence of the presence of fibres, especially steel ones, on the propagation of ultrasonic waves. The comparison of the Δv results after the destruction was not reliable, because they were influenced not only by the material itself but also by the destruction process.

The measures of variability of apparent velocities are shown by the standard deviation (SD) and the coefficient of variation (CV). There were large differences, even more than ten times, between these values for the cubes before and after the failure. The standard deviation before

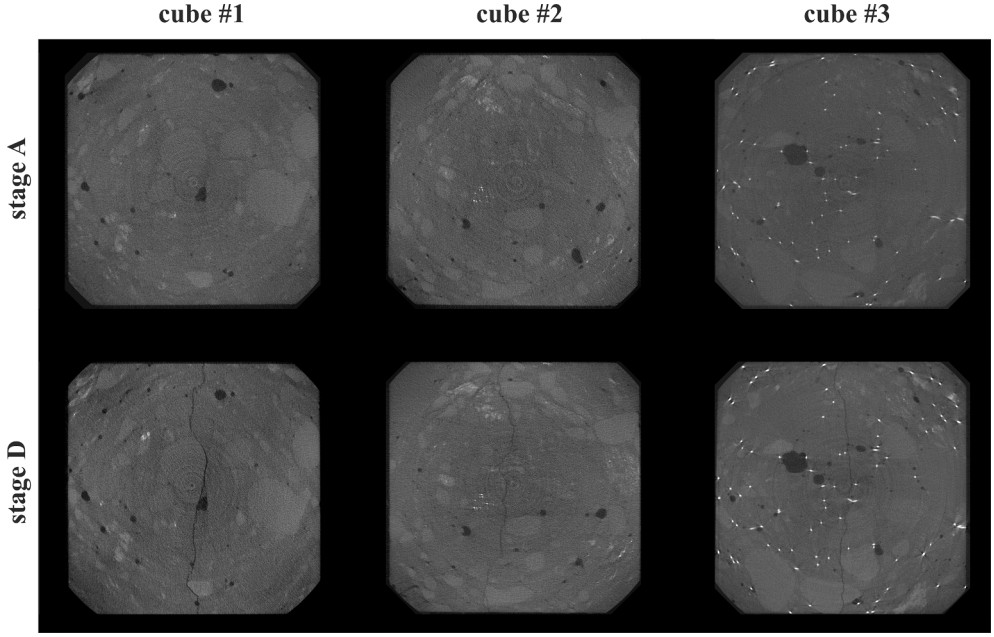

Fig. 10. X-ray micro-CT images of cubes #1–#3 before the test (stage A) and after fracture (stage D).

Table 1
Results of average apparent velocities of wave propagation determined by the starting point search (SPS) method for cubes #1–#3.

No. transmitter	Cube #1 (plain concrete)				Cube #2 (polymer fibres)				Cube #3 (steel fibres)			
	A	B	C	D	A	B	C	D	A	B	C	D
	[m/s]	[m/s]	[m/s]	[m/s]	[m/s]	[m/s]	[m/s]	[m/s]	[m/s]	[m/s]	[m/s]	[m/s]
T_1	4636.1	4699.4	3684.0	3715.3	4517.7	4377.7	3069.3	3033.6	4679.7	4637.4	3471.3	3664.7
T_2	4618.0	4695.1	3660.5	3653.3	4545.0	4569.4	3277.4	3333.1	4716.2	4677.2	3484.1	3515.7
T_3	4713.0	4681.0	3591.7	3628.9	4614.2	4627.6	3474.5	3470.1	4492.9	4435.6	3449.2	3450.2
T_4	4615.4	4615.5	3567.2	3683.8	4582.1	4576.9	3516.8	3512.5	4534.6	4520.7	3539.6	3977.4
T_5	4640.2	4637.7	3595.4	3628.9	4613.7	4577.9	3569.5	3517.8	4572.6	4544.1	3681.3	3624.7
T_6	4656.9	4584.6	3384.9	3434.7	4629.2	4498.8	3730.2	3708.4	4607.5	4619.4	3611.0	3615.5
T_7	4577.2	4642.6	2593.6	2645.8	4705.6	4690.2	2569.8	2695.3	4729.9	4692.6	2397.6	2618.2
T_8	4609.0	4603.1	2491.0	2519.2	4666.2	4632.8	2441.7	2554.7	4752.3	4746.8	2605.4	2737.2
T_9	4602.8	4580.2	2343.8	2482.8	4535.1	4604.3	2467.6	2489.3	4633.3	4690.5	2398.1	2685.8
T_{10}	4608.9	4604.8	2446.2	2477.2	4661.8	4657.8	2507.3	2552.5	4597.2	4649.2	2555.0	2700.3
T_{11}	4693.0	4641.7	2589.9	2589.5	4660.4	4694.6	2458.2	2390.1	4622.8	4597.7	2571.4	2875.7
T_{12}	4606.3	4625.5	2669.2	2651.5	4580.1	4534.0	2164.5	2237.8	4781.8	4786.6	2662.1	2840.8
Average [m/s]	4631.4	4634.3	3051.4	3092.6	4609.3	4586.8	2937.2	2957.9	4643.4	4633.1	3035.5	3192.2
Max value [m/s]	4713.0	4699.4	3684.0	3715.3	4705.6	4694.6	3730.2	3708.4	4781.8	4786.6	3681.3	3977.4
Min value [m/s]	4577.2	4580.2	2343.8	2477.2	4517.7	4377.7	2164.5	2237.8	4492.9	4435.6	2397.6	2618.2
Δv [m/s]	135.8	119.1	1340.3	1238.1	187.9	316.9	1565.7	1470.6	289.0	351.1	1283.7	1359.2
SD [m/s]	39.3	40.3	563.0	561.7	58.7	88.5	555.9	526.5	89.7	98.4	535.0	489.5
CV	0.8	0.9	18.4	18.2	1.3	1.9	18.9	17.8	1.9	2.1	17.6	15.3

damage (states A and B) ranged from 39.3 m/s to 98.4 m/s. After damage (stages C and D), the SD ranged from 489.5 m/s to 563.0 m/s. What is worth noting, the smallest difference between the state before and after the failure was observed for the sample with steel fibres. The values of the coefficient of variation for undamaged cubes #1-#3 were respectively 0.8%, 1.3% and 1.9% for stage A and 0.9%, 1.9% and 2.1% for stage B. This indicates a slight variability in the velocity of wave propagation along the considered paths. These ratios increased to 18.4 %, 18.9% and 17.6% for stage C and 18.2%, 17.8% and 15.3% for stage D, which proves that the continuity of the samples was interrupted and the wave travel was disturbed.

5. Discussion

The analysis of the results presented in the previous section allows discussing some important aspects connected with advantages, limitations and practical application in fracture imaging. The main advantage of ultrasound tomography is the ability to visualize the internal structure of engineering structure elements on the basis of measurements carried out on their surface. The method can be applied in situ on real objects. It can be used in both periodic checking and monitoring modes, which makes this method quite universal. In periodic inspections, it is preferable to use ultrasonic transducers with dry coupling as a quick and reliable approach. In such a way, several places can be easily and effectively inspected. In the monitoring mode, it will be more convenient to use PZT transducers installed permanently, as presented in this study. Another advantage is the fact that ultrasound tomography imaging of concrete fracture basically does not require any reference data. This can be treated as a baseline-free approach as any crack in concrete will result in significant differences in wave propagation velocities on ultrasound tomography maps.

The presented method also has some disadvantages and limitations of use. First of all, the ultrasound tomography algorithm is sensitive to the imprecise determination of the time-of-flight. Large inaccuracies in the TOF determination can lead to incorrect tomography imaging. To avoid this problem, a novel, reliable method of TOF determination has been developed in this study. Another issue is connected with the precision of imaging. It is worth noting that the resolution of the tomographic velocity images is closely related to the number of measurement points and paths. In ultrasound tomography, a tested sample is first divided into geometric cells called pixels. Each pixel represents a discrete area with an associated intensity value (here: wave propagation velocity). Only a sufficiently large amount of collected measurement data will enable the reconstruction of the internal structure with reasonable accuracy. In this study, the tomographic velocity images consisted of 36 pixels which guaranteed the identification of the existence and location of the fracture which coincided with the real course of the cracks obtained from micro-CT. Crack opening width was not possible to obtain in this research, mainly due to limited measurements in the selected time instances.

The practical application of the proposed method requires the consideration of some aspects. In a real situation, the method can be advantageously used to monitor critical places in concrete structures of special importance, such as bridges, tall buildings, halls or stadiums. Another issue is connected with the equipment necessary to conduct measurements. Generally, ultrasound tomography does not require any complex devices. However, one aspect is important, especially in the monitoring mode. In classical ultrasonic methods, usually one PZT transducer is used as an actuator and the others are used as sensors. In ultrasound tomography, the situation is different because several actuators are used that must be triggered sequentially. This requires the design of a special measuring system that will be able to automatically trigger all actuators one after the other. In the presented research, the actuators were manually switched, which made it impossible to automatically monitor the entire splitting process. Designing a measuring system with full control of each channel would allow determining the exact time of starting the fracture process and detecting the start time of the crack.

6. Conclusions

This paper presents the results of non-destructive testing of concrete elements based on ultrasonic waves. A novel method of TOF determination was proposed. The superiority of the proposed SPS method is related to the precise time-of-flight calculation and avoidance of the error associated with a selected time window.

The investigations proved that ultrasound transmission tomography can be effectively used in the imaging of the internal structure of concrete elements. It was observed that tomographic velocity images enabled the characterization of elements made of different types of concrete, including concrete with fibres. Compared to cubes made of plain concrete, an increase in the average velocity of wave propagation in concrete with steel fibres was observed, and a decrease – in concrete with polymer fibres. Moreover, the efficiency of imaging the internal

structure of concrete elements at different stages of mechanical degradation using ultrasonic tomography was demonstrated. It was possible to reconstruct areas with cracks in all tested specimens, regardless of the type of concrete mixture used to make the samples.

Ultrasound transmission tomography has great potential to be used in monitoring systems of concrete structures, aimed at the assessment of the fracture process. Future works should be directed into the design of an automated system for excitation, registration and processing of ultrasonic data to obtain tomographic images in real-time.

CRediT authorship contribution statement

Monika Zielińska: Conceptualization, Methodology, Software, Formal analysis, Visualization, Writing – original draft. **Magdalena Rucka:** Conceptualization, Methodology, Investigation, Formal analysis, Writing – review & editing, Supervision, Project administration, Funding acquisition.

Declaration of Competing Interest

The authors declare that they have no known competing financial interests or personal relationships that could have appeared to influence the work reported in this paper.

Acknowledgements

The study was financed by the National Science Centre, Poland, under the project "Complex investigations of the development of micro- and macro-cracks in concrete members using elastic waves: experiments and discrete element method modelling" no 2019/35/B/ST8/01905. The authors would like to thank Prof. Łukasz Skarżyński for providing micro-CT images used in this study to compare with the results of ultrasound tomography (the images were used in Fig. 10).

References

[1] Ł. Skarżyński, J. Tejchman, Experimental investigations of fracture process in concrete by means of X-ray micro-computed tomography, Strain 52 (1) (2016) 26–45.
[2] Ł. Skarżyński, I. Marzec, J. Tejchman, Fracture evolution in concrete compressive fatigue experiments based on X-ray micro-CT images, Int. J. Fatigue 122 (2019) 256–272.
[3] L. Mao, Z. Yuan, M. Yang, H. Liu, F. Chiang, 3D strain evolution in concrete using in situ X-ray computed tomography testing and digital volumetric speckle photography, Measurement 133 (2019) 456–467, https://doi.org/10.1016/j.measurement.2018.10.049.
[4] J. Suchorzewski, J. Tejchman, M. Nitka, Experimental and numerical investigations of concrete behaviour at meso-level during quasi-static splitting tension, Theor. Appl. Fract. Mech. 96 (2018) 720–739, https://doi.org/10.1016/j.tafmec.2017.10.011.
[5] E. Wojtczak, M. Rucka, Ł. Skarżyński, Monitoring the fracture process of concrete during splitting using integrated ultrasonic coda wave interferometry, digital image correlation and X-ray micro-computed tomography, NDT E Int. 126 (2022), 102591, https://doi.org/10.1016/j.ndteint.2021.102591.
[6] Ł. Skarżyński, K. Kibort, A. Małachowska, 3D X-Ray Micro-Ct Analysis of Rebar Corrosion in Reinforced Concrete Subjected To a Chloride-Induced Environment, Molecules 27 (2022) 1–12, https://doi.org/10.3390/molecules27010192.
[7] T. Ponikiewski, J. Katzer, M. Bugdol, M. Rudzki, X-ray computed tomography harnessed to determine 3D spacing of steel fibres in self compacting concrete (SCC) slabs, Constr. Build. Mater. 74 (2015) 102–108, https://doi.org/10.1016/j.conbuildmat.2014.10.024.
[8] T. Ponikiewski, J. Gołaszewski, M. Rudzki, M. Bugdol, Determination of steel fibres distribution in self-compacting concrete beams using X-ray computed tomography, Arch. Civ. Mech. Eng. 15 (2015) 558–568, https://doi.org/10.1016/j.acme.2014.08.008.
[9] Ł. Skarżyński, J. Suchorzewski, Mechanical and fracture properties of concrete reinforced with recycled and industrial steel fibers using Digital Image Correlation technique and X-ray micro computed tomography, Constr. Build. Mater. 183 (2018) 283–299, https://doi.org/10.1016/j.conbuildmat.2018.06.182.
[10] D. Zheng, W. Song, J. Fu, G. Xue, J. Li, S. Cao, Research on mechanical characteristics, fractal dimension and internal structure of fiber reinforced concrete under uniaxial compression, Constr. Build. Mater. 258 (2020), 120351, https://doi.org/10.1016/j.conbuildmat.2020.120351.
[11] Ł. Skarżyński, Mechanical and radiation shielding properties of concrete reinforced with boron-basalt fibers using Digital Image Correlation and X-ray micro-computed tomography, Constr. Build. Mater. 255 (2020) 119252.
[12] Y. Huang, D. Yan, Z. Yang, G. Liu, 2D and 3D homogenization and fracture analysis of concrete based on in-situ X-ray Computed Tomography images and Monte Carlo simulations, Eng. Fract. Mech. 163 (2016) 37–54, https://doi.org/10.1016/j.engfracmech.2016.06.018.
[13] W. Trawiński, J. Bobiński, J. Tejchman, Two-dimensional simulations of concrete fracture at aggregate level with cohesive elements based on X-ray μCT images, Eng. Fract. Mech. 168 (2016) 204–226, https://doi.org/10.1016/j.engfracmech.2016.09.012.
[14] Z. Yang, W. Ren, R. Sharma, S. McDonald, M. Mostafavi, Y. Vertyagina, T. J. Marrow, In-situ X-ray computed tomography characterisation of 3D fracture evolution and image-based numerical homogenisation of concrete, Cem. Concr. Compos. 75 (2017) 74–83, https://doi.org/10.1016/j.cemconcomp.2016.10.001.
[15] M. Nitka, J. Tejchman, A three-dimensional meso-scale approach to concrete fracture based on combined DEM with X-ray μCT images, Cem. Concr. Res. 107 (2018) 11–29, https://doi.org/10.1016/j.cemconres.2018.02.006.
[16] Ł. Skarżyński, I. Marzec, Shear fracture of longitudinally reinforced concrete beams under bending using Digital Image Correlation and FE simulations with concrete micro-structure based on X-ray micro-computed tomography images, Constr. Build. Mater. 274 (2021) 122116.
[17] Ł. Skarżyński, J. Tejchman, Tejchman, Experimental investigations of damage evolution in concrete during bending by continuous micro-CT scanning, Mater. Charact. 154 (2019) 40–52.
[18] Ł. Skarżyński, J. Tejchman, Investigations on fracture in reinforced concrete beams in 3-point bending using continuous micro-CT scanning, Constr. Build. Mater. 284 (2021) 122796.
[19] D. Lluveras, M.Á. Molero-armenta, Á. Miguel, M. Gonz, J. Anaya, Ultrasound Transmission Tomography for Detecting and Measuring Cylindrical Objects Embedded in Concrete, (2017). https://doi.org/10.3390/s17051085.
[20] S. Beniwal, D. Ghosh, A. Ganguli, Ultrasonic imaging of concrete using scattered elastic wave modes, NDT E Int. 82 (2016) 26–35, https://doi.org/10.1016/j.ndteint.2016.04.003.
[21] V.G. Haach, F.C. Ramirez, Qualitative assessment of concrete by ultrasound tomography, Constr. Build. Mater. 119 (2016) 61–70, https://doi.org/10.1016/j.conbuildmat.2016.05.056.
[22] K. Schabowicz, Ultrasonic tomography - The latest nondestructive technique for testing concrete members - Description, test methodology, application example, Arch. Civ. Mech. Eng. 14 (2014) 295–303, https://doi.org/10.1016/j.acme.2013.10.006.
[23] M. Zielińska, M. Rucka, Detection of debonding in reinforced concrete beams using ultrasonic transmission tomography and hybrid ray tracing technique, Constr. Build. Mater. 262 (2020), 120104, https://doi.org/10.1016/j.conbuildmat.2020.120104.
[24] P. Choi, D.H. Kim, B.H. Lee, M.C. Won, Application of ultrasonic shear-wave tomography to identify horizontal crack or delamination in concrete pavement and bridge, Constr. Build. Mater. 121 (2016) 81–91, https://doi.org/10.1016/j.conbuildmat.2016.05.126.
[25] T. Sanderson, K. Freeseman, Z. Liu, Concrete bridge deck overlay assessment using ultrasonic tomography, Case Stud. Constr. Mater. 16 (2022), e00878, https://doi.org/10.1016/j.cscm.2022.e00878.
[26] H.K. Chai, S. Momoki, Y. Kobayashi, D.G. Aggelis, T. Shiotani, Tomographic reconstruction for concrete using attenuation of ultrasound, NDT E Int. 44 (2011) 206–215, https://doi.org/10.1016/j.ndteint.2010.11.003.
[27] Z. Niu, W. Wang, X. Huang, J. Lai, Integrated assessment of concrete structure using Bayesian theory and ultrasound tomography, Constr. Build. Mater. 274 (2021), 122086, https://doi.org/10.1016/j.conbuildmat.2020.122086.
[28] V.G. Haach, L.M. Juliani, Application of ultrasonic tomography to detection of damages in concrete, Proc. Int. Conf. Struct. Dyn. , EURODYN. 2014-Janua (2014) 3351–3357.
[29] Z. Perkowski, K. Tatara, The use of Dijkstra's algorithm in assessing the correctness of imaging brittle damage in concrete beams by means of ultrasonic transmission tomography, Materials (Basel) 13 (2020) 551, https://doi.org/10.3390/ma13030551.
[30] S. Basu, A. Thirumalaiselvi, S. Sasmal, T. Kundu, Nonlinear ultrasonics-based technique for monitoring damage progression in reinforced concrete structures, Ultrasonics 115 (2021), 106472, https://doi.org/10.1016/j.ultras.2021.106472.
[31] M. Rucka, M. Zielińska, Wave propagation signals for ultrasonic tomography of concrete during splitting, Gdańsk University of Technology (2022), https://doi.org/10.34808/p2fs-5z67.
[32] E. Cescatti, L. Rosato, M.R. Valluzzi, F. Casarin, An Automatic Algorithm for the Execution and Elaboration of Sonic Pulse Velocity Tests in Direct and Tomographic Arrangements, Springer International Publishing (2019), https://doi.org/10.1007/978-3-319-99441-3.
[33] M.S. Beck, Correlation in instruments: cross correlation flowmeters., Instrum. Sci. Technol. 2, B.E. J (1981) 89–105.
[34] S. Herter, S. Youssef, M.M. Becker, S.C.L. Fischer, Machine Learning Based Preprocessing to Ensure Validity of Cross-Correlated Ultrasound Signals for Time-of-Flight Measurements, J. Nondestruct. Eval. 40 (2021) 1–9, https://doi.org/10.1007/s10921-020-00745-7.
[35] J.D. Rodríguez-Mariscal, J. Canivell, M. Solís, Evaluating the performance of sonic and ultrasonic tests for the inspection of rammed earth constructions, Constr. Build. Mater. 299 (2021) 123854.
[36] Z. Fang, R. Su, L. Hu, X. Fu, A simple and easy-implemented time-of-flight determination method for liquid ultrasonic flow meters based on ultrasonic signal

onset detection and multiple-zero-crossing technique, Meas. J. Int. Meas. Confed. 168 (2021), 108398, https://doi.org/10.1016/j.measurement.2020.108398.
[37] N. Maeda, A Method for Reading and Checking Phase Time in Auto-Processing System of Seismic Wave Data, Zisin (Journal Seismol. Soc. Japan. 2nd Ser.) 38 (3) (1985) 365–379.
[38] H. Choi, Y. Ham, J.S. Popovics, Integrated visualization for reinforced concrete using ultrasonic tomography and image-based 3-D reconstruction, Constr. Build. Mater. 123 (2016) 384–393, https://doi.org/10.1016/j.conbuildmat.2016.07.010.
[39] P.M.V. Subbarao, P. Munshi, K. Murlidhar, Performance evaluation of tomographic algorithms applied to reconstruction of a three dimensional temperature field, Numer. Heat Transf. Part B Fundam. 31 (1997).
[40] E.F. Oliveira, S.B. Melo, C.C. Dantas, D.A.A. Vasconcelos, L. Cadiz, Comparison Among Tomographic Reconstruction Algorithms With a Limited Data, Int. Nucl. Atl. Conf. - Ina. (2011).